Electron-impact double ionization of rare-gas ions

M. S. Pindzola,* D. C. Griffin,† and C. Bottcher
Atomic Theory Group, Physics Division, Oak Ridge National Laboratory, Oak Ridge, Tennessee 37830

D. H. Crandall,‡ R. A. Phaneuf, and D. C. Gregory
Experimental Atomic Physics Group, Physics Division, Oak Ridge National Laboratory, Oak Ridge, Tennessee 37830
(Received 3 November 1983)

Cross sections for the removal of two electrons from rare-gas ions by single collisions with incident electrons have been both measured using crossed beams of ions and electrons, and calculated using Hartree-Fock distorted-wave theory. For initial ions Ar^{4+}, Kr^{4+}, and Xe^{4+} the measured peak cross sections are 1.4×10^{-18}, 6.5×10^{-18}, and 9.0×10^{-18} cm^2, respectively. These measurements confirm and extend the measurements of Müller and Frodl and of Achenbach *et al.* Calculations were performed for the charge-state-4 + ions and for Xe^{+}, Xe^{2+}, and Xe^{3+}. Comparison of experiment and theory indicates that the double ionization of rare-gas ions is dominated by the indirect mechanism of inner-shell single ionization followed by autoionization. The distorted-wave calculations for the 4*d* ionization cross section of Xe^{q+} ($q=1$ to 4) ions are strongly influenced by term dependence in the ejected-electron continuum, and by ground-state correlations.

I. INTRODUCTION

Multiple ionization of atomic ions via single collisions with electrons has not been widely studied. Direct multiple ionization is anticipated to have a relatively small amplitude since a correlated multiple electron interaction is required. However, a single-ionization event ejecting an inner-shell electron can leave the product ion in an excited state which may subsequently cascade through several autoionizing levels resulting in relatively large net multiple ionization from a single collision.

The work of Müller and Frodl[1] clearly demonstrated the inner-shell ionization-autoionization mechanism for Ar ions. In addition their measurements suggested that the indirect mechanism of ionization-autoionization becomes progressively more dominant over direct multiple ionization for the more highly charged initial ions. The present experimental results extend measurements on double ionization to the next more highly charged ion, Ar^{4+}. The increasing dominance of ionization of a 2*p* electron followed by autoionization in the total double-ionization cross section, which was observed by Müller and Frodl for Ar^{+}, Ar^{2+}, and Ar^{3+} initial ions, is found in the present Ar^{4+} results.

Double ionization of Kr^{4+} and Xe^{4+} are also found to be consistent with ionization-autoionization as the primary production mechanism. However, the increasing complexity of the atomic structure of these ions results in significant contributions to double ionization from more than one inner-shell ionization. As a further complication in Xe^{4+}, the energy levels associated with the dominant 4*d* inner-shell ionization straddle the threshold for double ionization. The lower levels of the 4*d* vacancy configuration are true bound states and thus will contribute only to the single ionization of Xe.[4+] Even though experiment and theory differ by up to a factor of 2 in Xe^{4+}, the overall agreement found in the rare-gas ions encourages the ionization-autoionization interpretation.

Hartree-Fock distorted-wave calculations were made for various inner-shell ionization cross sections in Ar^{4+}, Kr^{4+}, and Xe^{q+} ($q=1$ to 4). The distorted-wave formalism[2,3] for electron-impact ionization is based on the Born approximation and involves both a triple partial-wave expansion of the incident, ejected, and scattered electron wave functions, and an average over the quantum numbers of the target configuration. As found in previous rk[4] on Xe^{+}, the ^1P term of the $4d^9kf$ ejected-electron continuum in the Xe ions is quite different from the other *LS* multiplets in the configuration. Thus for members of the Xe isonuclear sequence, we modified our configuration-average ionization code to take into account term dependence in the ejected-electron continuum. We also included ground-state correlations for the Xe ions. We compare our calculations with the present measurements and the recent experimental results of Achenbach *et al.*[5]

II. EXPERIMENTAL APPROACH

The electron-ion crossed-beams technique has been described several times. The present arrangement corresponds to a recent description[6] with only a minor change in the analyzer.

The ions are extracted from the ORNL-PIG source (Oak Ridge National Laboratory Penning ion gauge configuration) and selected according to mass-to-charge ratio in crossed electric and magnetic fields. After transport of the beam to the collision chamber an electrostatic parallel-plate analyzer is used to remove ions whose charges have changed in the transport flight path. The electron and ion beams are crossed at 90° and a second parallel-plate analyzer separates the product (ionized) ions

from the incident ions. The only difference from the recent description of the apparatus[6] is that, for the present case, the ratio of charges of incident to product ions is $\frac{2}{3}$ and the spacing of analyzer exit holes is adjusted correspondingly. The flight path from the beams crossing point to the analyzer is just over 5 cm, so that, for typical ion velocities of 5×10^7 cm/sec, the time between collision and analysis is more than 0.1 μsec. This time is relatively long compared to both typical autoionization times and radiative lifetimes for ions which are at least a few-times charged.

Uncertainties in the measured cross sections are the same as found in previous work,[6] except for counting statistics which apply to each individual measurement. Total absolute uncertainties in the present data are estimated to be $\pm8\%$ near the peak of the measured cross sections. This total uncertainty is the quadrature sum of counting statistics on the signal at 95% confidence level and systematic uncertainties in each of the measured parameters estimated at a comparable level of confidence.

III. THEORETICAL APPROACH

In order to interpret the double-ionization measurements on the rare-gas ions, we made Hartree-Fock distorted-wave calculations for the inner-shell ionization cross sections. Our general expression for the average ionization cross section (in atomic units) is given by

$$\sigma=\int_0^{E/2}\frac{32q_t}{k_i^3k_ek_f}\sum_{l_i,l_e,l_f}(2l_i+1)(2l_e+1)(2l_f+1)\times\left[\sum_\lambda A(l_i,l_e,l_f,\lambda)[R^\lambda(k_el_e,k_fl_f;n_tl_t,k_il_i)]^2+\sum_{\lambda'}B(l_i,l_e,l_f,\lambda')[R^{\lambda'}(k_fl_f,k_el_e;n_tl_t,k_il_i)]^2-\sum_\lambda\sum_{\lambda'}C(l_i,l_e,l_f,\lambda,\lambda')R^\lambda(k_el_e,k_fl_f;n_tl_t,k_il_i)R^{\lambda'}(k_fl_f,k_el_e;n_tl_t,k_il_i)\right]d(\tfrac{1}{2}k_e^2)\,, \tag{1}$$

where the wave numbers k_i, k_e, and k_f and the angular momentum quantum numbers l_i, l_e, and l_f correspond to the incident, ejected and scattered electron, respectively. The continuum normalization is chosen as one times a sine function. The energy $E=\frac{1}{2}k_i^2-I$, I being the ionization potential and q_t is the occupation number for the n_tl_t inner subshell. In Eq. (1) $R^\lambda(ij;rt)$ is the usual Slater radial integral for the Coulomb interaction between electrons, and the angular coefficients A, B, and C may be expressed in terms of standard 3-j and 6-j symbols, as found in previous work.[4] The maximum interference approximation of Peterkop[7] requires that the angular coefficient C must be chosen to be positive and real.

Several Hartree-Fock relativistic[8] atomic-structure calculations[9] were made in order to determine excitation energies and ionization potentials for the various rare-gas ions. As shown in Table I and Fig. 1, the main ionization-autoionization contribution to the double ionization of Ar^{4+} is expected to be the creation of a $2p$ vacancy configuration of Ar^{5+}. Similar $2p$ vacancy configurations will also contribute to the double ionization of Ar^{2+} and Ar^{3+} (Ref. 1). The largest ionization-autoionization contributions to the double ionization of Kr^{4+} are predicted to come from $3d$ and $3p$ vacancy configurations, as shown in Table I and Fig. 2. For vacancy configurations near the ionization potential of the next higher stage of ionization, we determine not only a configuration-average energy, but the spread in energy associated with the different *LSJ* levels of the configuration. The levels of the $3d$ vacancy configuration of Kr^{5+} all lie above the Kr^{6+} ionization potential, and thus all may autoionize. As seen in Fig. 3, the $4d$ vacancy configuration of Xe^{5+} straddles the Xe^{6+} ionization potential. On the basis of our atomic-structure calculations, we estimate that 50 of the 150 *LSJM* states present in the $4d^95p^2$ configuration are able to autoionize and thus contribute to the double ionization of Xe^{4+}. For Xe^+, Xe^{2+}, and Xe^{3+}, however, all the levels of the $4d$ vacancy configuration can autoionize. One should also note that deeper inner-shell vacancy configurations may have branching decay routes to several different ionization stages. However, their contribution to double ionization is small when compared to

TABLE I. Excitation energies relative to the ground level of the 4+ ion for various rare-gas ions in the configuration-average Hartree-Fock relativistic approximation.

Atomic ion	Configuration	Energy (eV)
Ar^{4+}	$2p^63s^23p^2$	0.0
Ar^{5+}	$2p^63s^23p$	73.7
Ar^{6+}	$2p^63s^2$	164.8
Ar^{6+}	$2p^63s\,3p$	179.8
Ar^{7+}	$2p^63s$	288.0
Ar^{5+}	$2p^53s^23p^2$	322.8
Kr^{4+}	$3p^63d^{10}4s^24p^2$	0.0
Kr^{5+}	$3p^63d^{10}4s^24p$	63.4
Kr^{6+}	$3p^63d^{10}4s^2$	141.2
Kr^{5+}	$3p^63d^94s^24p^2$	153.5
Kr^{6+}	$3p^63d^94s^24p$	234.7
Kr^{7+}	$3p^63d^{10}4s$	249.1
Kr^{5+}	$3p^53d^{10}4s^24p^2$	280.5
Xe^{4+}	$4p^64d^{10}5s^25p^2$	0.0
Xe^{5+}	$4p^64d^{10}5s^25p$	53.6
Xe^{5+}	$4p^64d^95s^25p^2$	117.1
Xe^{6+}	$4p^64d^{10}5s^2$	118.9
Xe^{6+}	$4p^64d^95s^25p$	184.9
Xe^{7+}	$4p^64d^{10}5s$	209.5
Xe^{5+}	$4p^54d^{10}5s^25p^2$	210.9

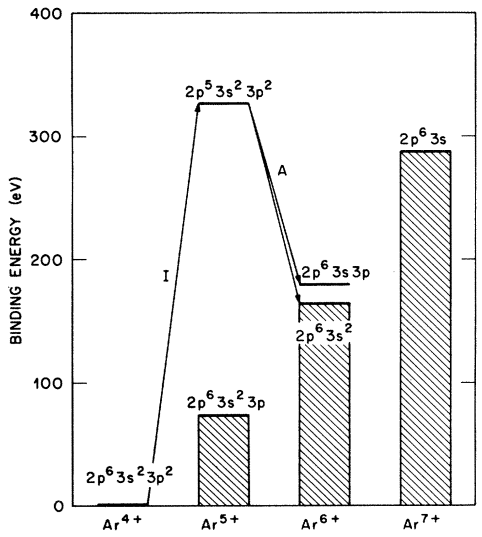

FIG. 1. Energy-level diagram for double ionization of Ar^{4+}. The arrowed line marked I is an inner-shell ionization path. The arrowed lines marked A are autoionization paths.

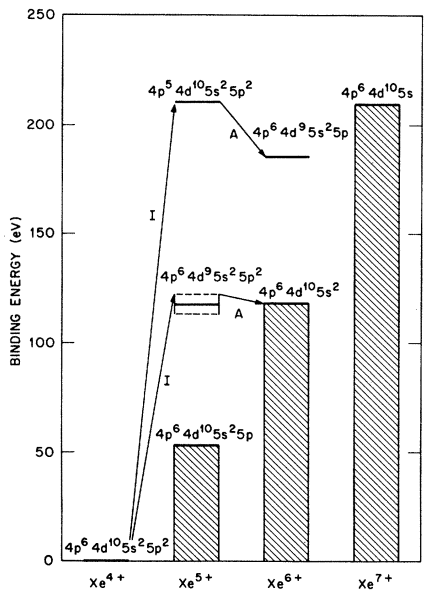

FIG. 3. Energy-level diagram for double ionization of Xe^{4+}. The arrowed lines marked I are inner-shell ionization paths. The arrowed lines marked A are autoionization paths.

the vacancy configurations shown in Figs. 1—3. Further, it is energetically possible for some of inner-shell vacancies shown in Figs. 1—3 to decay to ionization stages with a net of three electrons removed. However, these higher ionization stages are not accessed by sequential two-electron interactions, and thus their effect on the branching ratio for double ionization is presumed to be small.

We used Hartree-Fock bound-state orbitals[10] to construct distorted-wave potentials for the hundreds of continuum wave functions needed to evaluate Eq. (1) for the various inner-shell ionization cross sections. The radial Schrödinger equation for continuum orbitals, $P_{kl}(r)$, is given by

$$\left[-\frac{1}{2}\frac{d^2}{dr^2}+\frac{l(l+1)}{2r^2}-\frac{Z}{r}+V_{\rm HF}-\frac{k^2}{2}\right]P_{kl}(r)=0\,, \qquad (2)$$

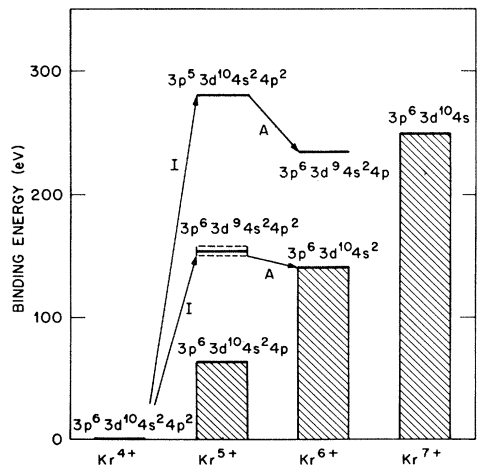

FIG. 2. Energy-level diagram for double ionization of Kr^{4+}. The arrowed lines marked I are inner-shell ionization paths. The arrowed lines marked A are autoionization paths.

where Z is the atomic number and $V_{\rm HF}$ is the Hartree-Fock operator containing both direct and nonlocal-exchange integrals. For most continuum wave functions the configuration-average Hartree-Fock operator, approximated by a local Hartree plus semiclassical-exchange (SCE) potential,[11] is adequate for substitution into Eq. (2). For the $4d$ inner-shell ionization of the Xe^{q+} ($q=1$—4) ions, however, the important $4d^9 kf\,{}^1P$ ejected-electron continuum is completely misrepresented by the SCE potential. This is caused by the large positive dipole-exchange integral in the ^1P term-dependent Hartree-Fock operator, given by the expression

$$V^{^1P}_{\rm HF}=V^{\rm CA}_{\rm HF}-\tfrac{8}{35}J^2_{4d}-\tfrac{2}{21}J^4_{4d}+\tfrac{137}{70}K^1_{4d}-\tfrac{2}{105}K^3_{4d}-\tfrac{5}{231}K^5_{4d}\,, \qquad (3)$$

where $V^{\rm CA}_{\rm HF}$ is the configuration-average operator, and J^ν and K^ν are the usual direct and exchange integrals.

As a guide in studying term-dependent effects, it is useful to introduce the effective local potential $V_{\rm eff}(r)$, which for the Hartree-Fock equations is given by

$$V_{\rm eff}(r)=\frac{l(l+1)}{2r^2}-\frac{Z}{r}+\frac{1}{r}Y(kl;r)+\frac{1}{r}\frac{X(kl;r)}{P_{kl}(r)}\,, \qquad (4)$$

where we use a notation similar to Fischer's;[10] $Y(kl;r)/r$ is the direct potential and $X(kl;r)/r$ is the exchange function. A simple linear interpolation may be used so that singularities in $V_{\rm eff}(r)$ do not appear in graphical display. We must emphasize that we only use $V_{\rm eff}(r)$ as a descriptive device; all term-dependent continuum orbitals used in this paper are solutions to Eq. (2) with the nonlocal Hartree-Fock operator.

We plot configuration-average (CA) and term-dependent effective potentials and continuum orbitals for both Xe^+ and Xe^{2+} in Fig. 4. For Xe^+ the configuration-average effective potential has a small nega-

tive barrier, while the ^1P term-dependent potential has a large positive barrier caused in part by the contribution from the positive dipole-exchange integral. The difference in the two potentials has a dramatic effect on the shape of low-energy continuum orbitals. In Fig. 4(a) the first antinode of the kf orbital at an energy of 1 eV is located in the inner-well region of the configuration-average potential and overlaps strongly with the $4d$ bound orbital. In Fig. 4(b) the first antinode of the kf orbital at the same energy of 1 eV is located in the outer-well region of the ^1P term-dependent potential and overlaps only weakly with the $4d$ bound orbital.

The photoionization cross section is a direct measure of the ejected-electron continuum. The $4d$ photoionization cross section is directly proportional to the radial dipole integral $\langle kf \mid r \mid 4d \rangle$, which measures the $4d$ overlap with the kf orbital. In Fig. 5 we plot the $4d$ cross section for neutral Xe and the Xe^{q+} ions ($q=1$–4). At 1 eV above the threshold for photoionization of Xe^+, the configuration-average cross section is approximately 38×10^{-18} cm^2, while the ^1P term-dependent cross section is much lower at 14×10^{-18} cm^2. The same dramatic change in the predicted neutral Xe cross section caused by including term dependence in the continuum has been pointed out by Starace.[13]

For Xe^{2+} the barrier has disappeared altogether in the configuration-average effective potential, while the ^1P term-dependent potential still has a small positive barrier. In Fig. 4(c) the first antinode of the kf orbital has moved deeper into the inner-well region of the configuration-average potential and its overlap with the $4d$ has begun to wash out due to wave cancellation. In Fig. 4(d) the first antinode of the kf orbital has also moved further toward the nucleus in relation to Fig. 4(b), but this has caused its overlap with the $4d$ orbital to increase. At 1 eV above the threshold for photoionization of Xe^{2+}, the predicted

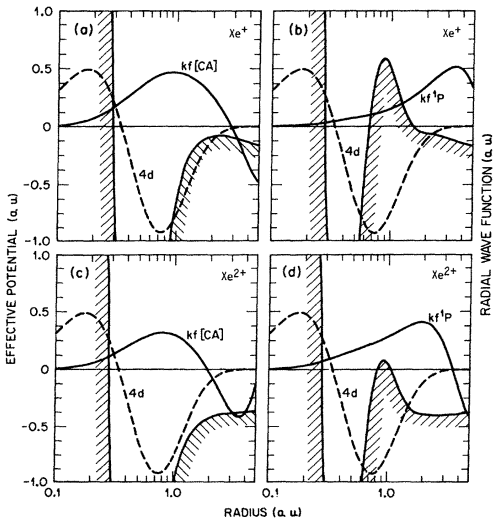

FIG. 4. Configuration-average and term-dependent effective potentials and continuum orbitals for (a) or (b), Xe^+, and (c) or (d), Xe^{2+}. Hatched solid curves, effective potentials; solid curves labeled kf, continuum orbitals at 1.0 eV; dashed curves labeled $4d$, $4d$ bound orbitals.

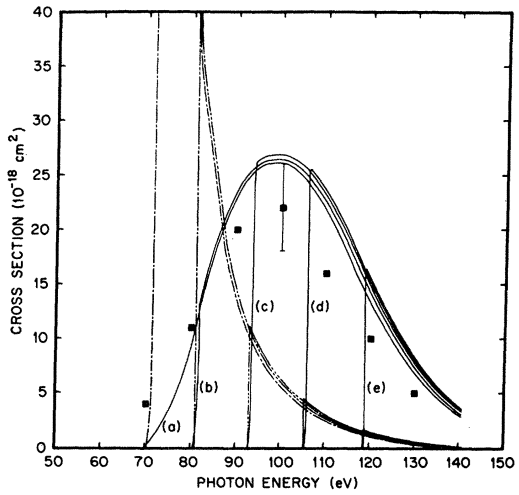

FIG. 5. $4d$ inner-shell photoionization cross sections for Xe and Xe^{q+} ions ($q=1$–4). Chained curves are configuration-average results. Solid curves are ^1P term-dependent results including ground-state correlations. Ionization thresholds are (a) Xe at 70 eV, (b) Xe^+ at 81 eV, (c) Xe^{2+} at 93 eV, (d) Xe^{3+} at 105 eV, and (e) Xe^{4+} at 119 eV. ■, experimental measurements for neutral Xe (Ref. 12).

configuration-average cross section is approximately 10×10^{-18} cm^2, while the ^1P term-dependent cross section is now higher at 26×10^{-18} cm^2. The wave mechanical mechanism that causes term-dependent effects to lower the near-threshold photoionization cross section for neutral Xe and Xe^+, while raising the cross section for higher stages of ionization, will similarly influence the electron-impact ionization cross section.

Whenever term-dependent effects were suspected to be important in electron-impact ionization, separate ejected-electron partial cross sections were calculated using term-dependent and configuration-average potentials and then added and subtracted[4] from the total cross section obtained using Eq. (1) and SCE continuum orbitals. As pointed out by Younger,[14] ground-state pair correlations will also be important in ejected-electron continua exhibiting strong term dependence. For the Xe^{q+} ions ($q=1$–4) as outlined in previous work,[4] the important $4d\rightarrow4f$ ground-state pair correlations were included through the use of multiconfiguration Hartree-Fock wave functions.[10] When needed, the relatively small contributions to the total cross section made by direct double ionization were estimated using the binary-encounter approximation.[15]

IV. COMPARISON OF EXPERIMENT AND THEORY

The complete data for electron-impact double ionization of Ar^{4+} are listed in Table II and plotted in Fig. 6. Energy-level calculations, summarized in Table I and Fig. 1, predict the double-ionization threshold for Ar^{4+} at 164.8 eV and the $2p$ ionization-autoionization threshold at 322.8 eV. The solid curve in Fig. 6 is a distorted-wave calculation for the $2p$ inner-shell ionization obtained using

TABLE II. Measured cross sections for double ionization of Ar^{4+} by electrons. Uncertainties shown are 1-standard-deviation (1 s.d.) reproducibility. Absolute uncertainty is about ±8% at the peak of the cross section.

Energy (eV)	Cross section (10^{-18} cm^2)
154	0.026±0.030
190	0.090±0.041
241	0.039±0.024
290	0.091±0.034
340	0.298±0.042
364	0.546±0.042
390	0.705±0.056
438	0.876±0.039
489	0.923±0.043
537	1.173±0.033
588	1.223±0.049
690	1.387±0.057
785	1.427±0.031
886	1.387±0.030
982	1.336±0.040
1181	1.280±0.038
1787	1.188±0.037

Eq. (1) and Hartree-Fock configuration-average continuum orbitals. Term-dependent effects in the ejected-electron continuum of Ar^{4+} should be small. The peak in the present experimental cross section at 1.4×10^{-18} cm^2 is about 33% above theory. Also plotted in Fig. 6 are the experimental measurements on Ar^{2+} and Ar^{3+} by Müller and Frodl.[1] Comparison of the results for the Ar ions demonstrates increasing dominance of the $2p$ ionization-autoionization mechanism in the double-ionization cross section relative to direct double ionization as one goes to higher initial stages of ionization. It is not clear that the double ionization of Ar^{4+} should have a higher peak value than for Ar^{2+} and Ar^{3+}. In fact it would be anticipated

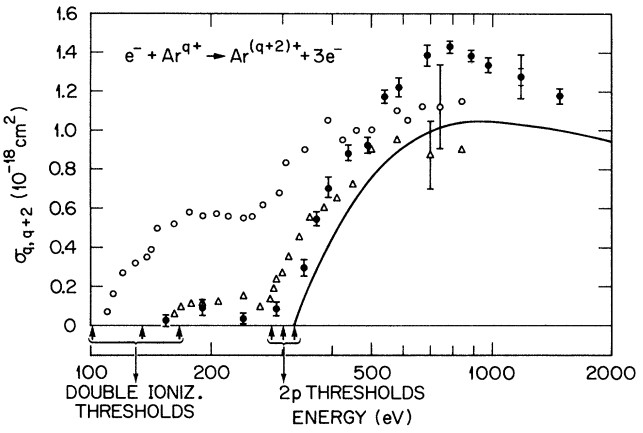

FIG. 6. Comparison of electron-impact double-ionization cross sections for the Ar isonuclear sequence. ○, experimental measurements for Ar^{2+} (Ref. 1). △, experimental measurements for Ar^{3+} (Ref. 1). ●, present measurements for Ar^{4+} with absolute uncertainty shown only on the point near 1200 eV. Solid curve is a distorted-wave calculation for the $2p$ ionization of Ar^{4+}. Arrows designate double-ionization threshold and $2p$ inner-shell ionization thresholds.

TABLE III. Measured cross sections for double ionization of Kr^{4+} by electron impact. Uncertainties shown are 1 s.d. reproducibility only. Total absolute uncertainty is about ±8% at the peak of the cross section.

Energy (eV)	Cross section (10^{-18} cm^2)
124.0	−0.023±0.066
137.4	−0.011±0.034
142.6	−0.024±0.030
145.0	+0.020±0.038
147.4	+0.080±0.045
149.4	0.090±0.049
150.8	0.222±0.038
152.3	0.265±0.056
153.4	0.279±0.035
155.4	0.392±0.050
158.4	0.447±0.049
162.5	0.642±0.038
167.0	0.738±0.046
173.2	1.167±0.070
183.2	1.490±0.070
192.9	1.824±0.056
202.7	2.100±0.067
213.0	2.453±0.063
217.2	2.547±0.072
221.5	2.880±0.048
232.0	3.105±0.049
242.3	3.535±0.050
250.8	3.563±0.066
262.3	4.010±0.075
271	4.215±0.064
291	4.615±0.053
312	4.948±0.070
342	5.208±0.078
391	5.557±0.073
440	5.706±0.067
490	5.838±0.048
538	5.871±0.077
588	5.929±0.073
606	6.112±0.064
638	6.310±0.072
687	6.470±0.045
736	6.334±0.071
785	6.383±0.060
835	6.313±0.067
884	6.236±0.065
983	6.115±0.044
1181	6.147±0.050
1478	5.834±0.043

that Ar^{4+} should have the smallest cross section due to decreasing direct ionization. It is possible that the apparent departure from expected ordering of the measured cross sections is due to real differences in the absolute calibration of the experiments.

In Table III and Fig. 7 complete data for double ionization of Kr^{4+} are presented. Energy-level calculations, summarized in Table I and Fig. 2, predict the double-ionization threshold for Kr^{4+} at 141.2 eV, the $3d$ ionization threshold at 153.5 eV, and the $3p$ ionization threshold at 280.5 eV. The solid curve in Fig. 7 is a distorted-wave

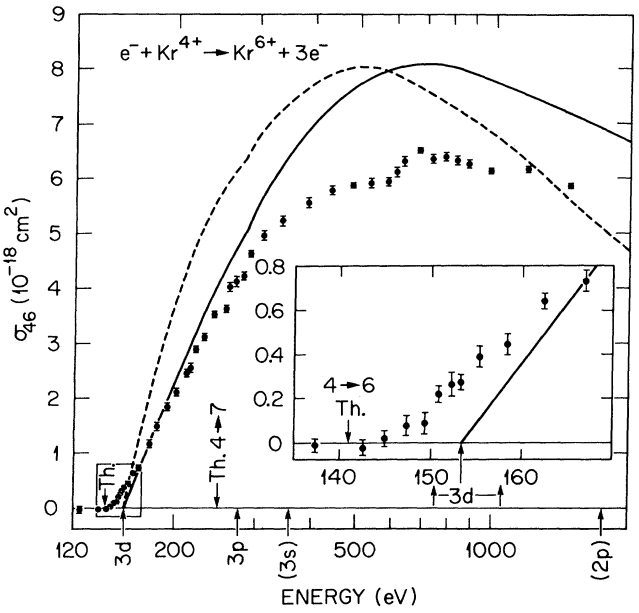

FIG. 7. Electron-impact double-ionization cross section for Kr^{4+}. ●, present measurements. Solid curve is a distorted-wave calculation for the 3*d* and 3*p* ionization. Dashed curve is the Lotz formula prediction for the 3*d* and 3*p* ionization. Arrows designate double-and triple-ionization thresholds and inner-shell ionization thresholds.

calculation for the 3*d* and 3*p* inner-shell ionizations obtained using Hartree-Fock configuration-average continuum orbitals. Term-dependent effects in the ejected-electron continuum of Kr^{4+} should be small. The dashed curve is the prediction of the Lotz semiempirical formula[16] for the ionization of the 3*d* and 3*p* inner shells. The distorted-wave calculations are seen to be in better agreement with the experimental data in the 175—400-eV range than the Lotz predictions. The experimental peak at 6.5×10^{-18} cm^2, however, is about 20% below theory. From the measurements in the region between the double-ionization threshold at 141.2 eV and the lowest 3*d* threshold near 150 eV, the relative importance of direct double ionization is seen to be small.

The small feature in the measured cross section near 600 eV remains a mystery. We cannot identify any transition of an inner-shell electron which could be followed by a relaxing transition giving rise to this feature. We are reluctant to invoke any truly multiple interaction of electrons during a single collision because we anticipate that they should be negligible and because a quantitative representation of such a collective process is not available.

In Table IV and Fig. 8 complete data for double ionization of Xe^{4+} are presented. The 4*d* ionization energies straddle the double-ionization threshold for Xe^{4+} at 118.9 eV, as shown in Table I and Fig. 3, while the 4*p* ionization threshold is at 210.9 eV. Shown for comparison in Fig. 8 are the recent experimental measurements on Xe^{4+} by Achenbach *et al.*[5] The two sets of experimental results agree within the stated uncertainties. The solid curves which bracket experimental data in Fig. 8 are distorted-wave calculations for the 4*d* and 4*p* inner-shell ionization cross sections. The 4*d* cross section is obtained using

TABLE IV. Measured cross sections for double ionization of Xe^{4+} by electron impact. Uncertainties are (1 s.d.) reproducibility only. Total absolute uncertainty is about ±8% at the peak of cross section.

Energy (eV)	Cross section (10^{-18} cm^2)
110	−0.04±0.30
119	−0.07±0.06
123	0.10±0.09
129	0.78±0.08
134	1.53±0.11
136.5	1.72±0.10
139	2.33±0.11
141	2.53±0.10
144.5	3.09±0.07
149.5	5.79±0.06
153.5	4.96±0.11
159	5.79±0.06
163.5	6.66±0.11
169	7.37±0.11
174	7.85±0.11
179	8.40±0.12
183	8.72±0.07
193	9.15±0.11
203	9.14±0.10
213	9.07±0.08
223	9.23±0.11
233	9.20±0.07
242	9.18±0.10
252	8.88±0.16
272	8.60±0.16
292	8.49±0.09
311	8.40±0.10
331	8.12±0.10
351	7.88±0.09
371	7.85±0.09
391	7.70±0.06
440	7.25±0.08
489	7.16±0.06
588	6.69±0.05
687	6.07±0.08
816	5.19±0.06
984	4.49±0.07
1180	3.77±0.11
1478	3.40±0.06

Hartree-Fock term-dependent continuum orbitals, while the 4*p* cross section calculation uses only configuration-average orbitals. The upper solid curve contains contributions from all 4*d* levels, while the lower solid curve is found by multiplying the 4*d* contribution in the upper curve by the fraction of 4*d* states which autoionize (1/3). The collision strengths from the 4*d* levels, however, are not necessarily distributed statistically. A more accurate, but more complicated distorted-wave calculation for Xe^{4+} would sum level-by-level contributions, instead of averaging over the configuration as done in Eq. (1). Further refinements in theory beyond a level-to-level ionization calculation might include examination of contributions from the excitation of autoionizing states below the 4*p* threshold. Such states may contribute to the double-ionization

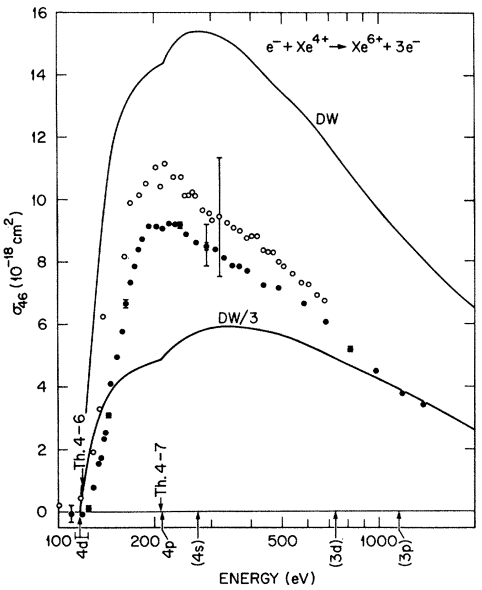

FIG. 8. Electron-impact double-ionization cross section for Xe^{4+}. ○, experimental measurements (Ref. 5). ●, present measurements. Upper solid curve, labeled DW, is a distorted-wave calculation for the 4*d* and 4*p* ionization. Lower solid curve, labeled DW/3, is a statistically scaled distorted-wave calculation for the 4*d* and 4*p* ionization. Arrows designate double- and triple-ionization thresholds, and inner-shell ionization thresholds.

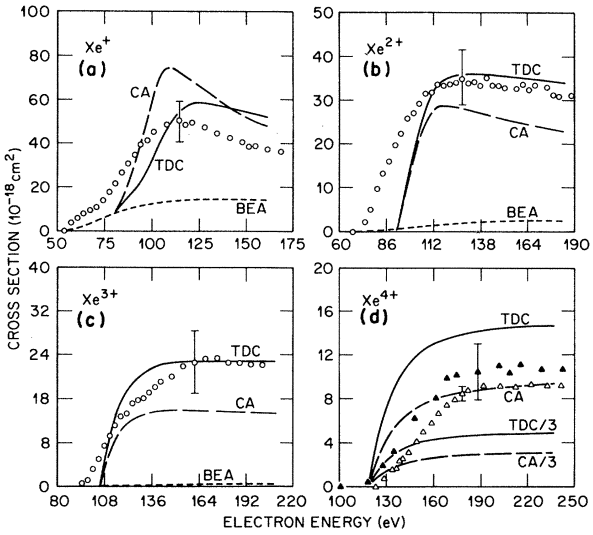

FIG. 9. Electron-impact double-ionization cross sections for (a) Xe^+, (b) Xe^{2+}, (c) Xe^{3+}, and (d) Xe^{4+}. ○ and ▲, experimental measurements (Ref. 5); △, present measurements; short-dashed curves labeled BEA, direct ionization using binary-encounter approximation; long-dashed curves labeled CA, 4*d* ionization using configuration-average wave functions plus direct ionization; solid curves labeled TDC, 4*d* ionization using term-dependent wave functions with ground-state correlations plus direct ionization.

cross section via excitation double autoionization.

In Fig. 9, the experiment and theory are compared for double ionization of atomic ions along the Xe isonuclear sequence in order to emphasize the importance of term dependence in the ejected-electron continuum. The experimental data of Achenbach *et al.*[5] are plotted for all the Xe^{q+} ions ($q = 1$–4), and the present measurements on Xe^{4+} are also included. The dotted curves labeled BEA are obtained by calculating the direct "double knockout" process in the binary-encounter approximation.[15] Although the binary-encounter approximation results are of dubious reliability, a full quantal calculation for the direct process would be difficult. As found in the Ar isonuclear sequence, the direct double-ionization process becomes completely negligible for ionization stages $q = 4$ and higher. The dashed curves labeled CA are found by adding a 4*d* ionization calculation using configuration-average scattering orbitals to the direct results. The solid curves labeled TDC include additional term-dependent and ground-state correlational effects as outlined in Sec. III. In Fig. 9(a), the term-dependent-correlated results for Xe^+ are lower than the configuration-average results and are in better agreement with the experiment. In Figs. 9(b) for Xe^{2+} and 9(c) for Xe^{3+}, on the other hand, the term-dependent-correlated results are higher than the configuration-average results but again are in better agreement with the experiment. The experimental verification that term-dependent effects lower the predicted cross section for Xe^+ but raise the cross section for all higher members of the isonuclear sequence is strong evidence for the wave mechanical mechanism proposed in Sec. III. In the Xe^{4+} case, as noted earlier, the scaling of the term-dependent calculation by 1/3 is based on the assumption that the collision strength is distributed statistically among the various 4*d* vacancy states, which may not be justified.

V. CONCLUSIONS

Our experimental and theoretical study of the rare-gas ions reveals that the double-ionization cross sections are reasonably well accounted for by the indirect process of inner-shell ionization followed by autoionization. Furthermore, the ionization-autoionization contributions from the 4*d* subshell of Xe ions are highly term dependent and proper radial continuum wave functions must be employed to obtain reliable results.

In recent years electron-ion scattering research has served to expand on the understanding gained from photoabsorption studies of term-dependent effects in heavy atomic systems. Electron-impact single-ionization studies have probed term dependence in autoionizing levels,[17] while the present double-ionization studies probe term dependence in the continuum.

ACKNOWLEDGMENTS

We would like to thank J. W. Hale for technical assistance with the ion source, Dr. R. D. Cowan for providing us with a copy of his atomic-structure program, and Dr. A. Müller for providing us with the Giessen group's experimental measurements prior to publication. This work was supported by the Office of Fusion Energy, U. S. Department of Energy under Contract No. W-7405-eng-26 with the Union Carbide Corporation.

*Permanent address: Department of Physics, Auburn University, Auburn, AL 36849.

†Permanent address: Department of Physics, Rollins College, Winter Park, FL 32789.

‡Permanent address: Office of Fusion Energy, Department of Energy, Washington, D.C. 20545.

[1]A. Müller and R. Frodl, Phys. Rev. Lett. 44, 29 (1980).

[2]D. L. Moores and H. Nussbaumer, J. Phys. B 3, 161 (1970).

[3]S. Younger, Phys. Rev. A 22, 111 (1980).

[4]M. S. Pindzola, D. C. Griffin, and C. Bottcher, J. Phys. B 16, L355 (1983).

[5]C. Achenbach, A. Müller, E. Salzborn, and R. Becker, Phys. Rev. Lett. 50, 2070 (1983).

[6]D. C. Gregory, P. F. Dittner, and D. H. Crandall, Phys. Rev. A 27, 724 (1983).

[7]R. K. Peterkop, Zh. Eksp. Teor. Fiz. 41, 1938 (1961); [Sov. Phys.—JETP 14, 1377 (1962)].

[8]R. D. Cowan and D. C. Griffin, J. Opt. Soc. Am. 66, 1010 (1976).

[9]R. D. Cowan, *The Theory of Atomic Structure and Spectra* (University of California, Berkeley, 1981).

[10]C. Froese Fischer, Comput. Phys. Commun. 14, 145 (1978); and *The Hartree-Fock Method for Atoms* (Wiley, New York, 1977).

[11]M. E. Riley and D. G. Truhlar, J. Chem. Phys. 63, 2182 (1975).

[12]J. B. West, P. R. Woodruff, K. Codling, and R. G. Houlgate, J. Phys. B 9, 407 (1976).

[13]A. Starace, Phys. Rev. A 2, 118 (1970).

[14]S. Younger, Phys. Rev. A 26, 3177 (1982).

[15]M. Gryzinski, Phys. Rev. 138, A336 (1965).

[16]W. Lotz, Z. Phys. 216, 241 (1968).

[17]M. S. Pindzola, D. C. Griffin, and C. Bottcher, Phys. Rev. A 27, 2331 (1983).